Interdecadal seesaw of precipitation variability between North China and the Southwest US

Article

Accepted Version

Interdecadal seesaw of precipitation variability between North China and the Southwest US

Qing Yang[1], Zhuguo Ma[1, 2], Peili Wu[3], Nicholas P. Klingaman[4], Lixia Zhang[5]

1. Key Laboratory of Regional Climate-Environment Research for Temperate East Asia, Institute of Atmospheric Physics, Chinese Academy of Sciences, Beijing, China
2. University of Chinese Academy of Sciences, Beijing, China
3. Met Office Hadley Centre, Exeter EX1 3PB, UK
4. National Centre for Atmospheric Science, Department of Meteorology, University of Reading, Reading, UK
5. The State Key Laboratory of Numerical Modeling for Atmospheric Sciences and Geophysical Fluid Dynamics (LASG), Institute of Atmospheric Physics, Chinese Academy of Sciences, Beijing, China

Submitted to *Journal of Climate*

Revised February 2019

Corresponding author: Dr. Zhuguo Ma

Key Laboratory of Regional Climate-Environment Research for Temperate East Asia, Institute of Atmospheric Physics, Chinese Academy of Sciences, Chao Yang District, Beijing, China

E-mail: mazg@tea.ac.cn. Tel: +86-10-82995047

Abstract

This paper reports a consistent seesaw relationship between interdecadal precipitation variability over North China and the Southwest United States (US), which can be found in observations and simulations with several models. Idealized model simulations suggest the seesaw could be mainly driven by the Interdecadal Pacific Oscillation (IPO), through a large-scale circulation anomaly occupying the entire northern North Pacific, while the Atlantic Multidecadal Oscillation (AMO) contributes oppositely and less. Modulation of precipitation by the IPO tends to be intensified when the AMO is in the opposite phase, but weakened when the AMO is in the same phase. The warm IPO phase is associated with an anomalous cyclone over the northern North Pacific and consequently, anomalous southwesterly winds bring more moisture and rainfall to the Southwest US, while northwesterly wind anomalies prevail over North China with negative rainfall anomalies. The east-west seesaw of rainfall anomalies reverses sign when the circulation anomaly becomes anticyclonic during the cold IPO phase. The IPO-related tropical SST anomalies affect the meridional temperature gradient over the North Pacific and adjacent regions and the mean meridional circulation. In the northern North Pacific, the atmospheric response to IPO forcing imposes an equivalent barotropic structure throughout the troposphere. An important implication from this study is the potential predictability of drought-related water stresses over these arid and semiarid regions, with the progress of our understanding and prediction of the IPO and AMO.

Key words: precipitation variability, interdecadal seesaw, Interdecadal Pacific Oscillation, drought, water resources

1. Introduction

Precipitation variability has profound impacts on society and ecosystems because it is closely related to drought, floods and water resources. Any useful prediction skills on precipitation will be greatly beneficial and normally associated with certain climate modes within the coupled climate system, such as the Interdecadal Pacific Oscillation (IPO; Zhang et al. 1997; Power et al. 1999) and the Atlantic Multidecadal Oscillation (AMO; Kerr 2000). The AMO, for example, is found to be strongly coupled with the global water cycle (Vellinga and Wu, 2004). Anthropogenic climate change is also affecting the global water cycle with regional impacts (Wu et al. 2013; 2015; Zhang et al. 2017; Kang and Eltahir, 2018). There are certain regions over the world, which are particularly sensitive to episodes of climate related precipitation variability on decadal or multidecadal timescales, such as North China and the Southwest United States (US).

Both North China and the Southwest US are typical arid and semi-arid regions, often hard hit by serious droughts. Many studies have attributed their interdecadal precipitation variability to the IPO, although the underlying mechanism of which is still under intensive debate (Farneti et al. 2014; Di Lorenzo et al. 2015; Newman et al. 2016; Si and Hu 2017; Henley 2017; Henley et al. 2017). The warm IPO phase corresponds to below-normal precipitation over North China (Ma and Shao 2006; Ma 2007; Zhou et al. 2013; Qian and Zhou 2014; Huang et al. 2017), but above-normal precipitation over the

Southwest US (Meehl and Hu 2006; Dai 2013), implying an obvious out-of-phase relationship for precipitation regime shift. Following the IPO cold-to-warm phase shift around 1977, there is an evident drying trend over North China, whereas a significant wetting trend is shown in the Southwest US since the 1950s; increased precipitation in the Huang-Huai River region (southern North China) after 2000, and a robust drying trend over the Southwest US since the 1980s are thought to be largely caused by the IPO warm-to-cold phase transition around 1999 (Ma 2007; Zhu et al. 2011; 2015; Dai 2013; Chylek et al. 2014; Qian and Zhou 2014). Additionally, the AMO contributes to the out-of-phase decadal precipitation pattern (Li and Bates 2007; Mo et al. 2009; Schubert et al. 2009; Feng et al. 2011; Zhu et al. 2016; Si and Ding 2016). The warm AMO phase tends to induce a stronger East Asia Summer Monsoon (EASM), leading to more northward transport of moisture and enhanced rainfall over North China, but dry conditions in the Southwest US (Lu et al. 2006; Sutton and Hodson 2005; 2007; Hu et al. 2011; Feng et al. 2011). The combined effects of the IPO and AMO are complicated and important (Schubert et al. 2009; Zhu et al. 2016; Si and Hu 2017; Yang et al. 2017). For instance, more than half (52%) of the spatial and temporal variance in multidecadal drought frequency over the US is attributable to the AMO and the Pacific Decadal Oscillation (PDO, Mantua et al. 1997; Mantua and Hare 2002), which is the North Pacific component of the IPO (McCabe et al. 2004).

The purposes of this study are to identify the interdecadal seesaw of precipitation variability between North China and the Southwest US, to further understand the associated formation mechanism related to the IPO and AMO, and to answer why there

87 is an out-of-phase decadal precipitation pattern between North China and the
88 Southwest US through analysis of decadal ocean forcings.
89 Although many studies have investigated the contrasting relationship of
90 precipitation variability between Asia and North America (e.g., Lau and Weng 2002;
91 Lau et al. 2004; Li et al. 2005; Ma and Fu 2007; Hua et al. 2011; Zhao et al. 2011; 2016;
92 Wang et al. 2014; Fang et al. 2014; 2015; Yang and Fu 2016; Zhu and Li 2016), the
93 circulation mechanism for the seesaw relationship remains unclear. This is because that
94 previous researches have focused on inconsistent study areas (Zhao et al. 2011; 2016;
95 Fang et al. 2015), time scales (Lau and Weng 2002; Lau et al. 2004; Fang et al. 2014;
96 Wang et al. 2014), and precipitation-related variables (Li et al. 2005; Yang and Fu
97 2016). Additionally, for attribution of precipitation variability, more attentions have
98 been paid to the Asian-Pacific Oscillation (Zhao et al. 2011; Fang et al. 2015), East
99 Asian subtropical monsoon heating (Zhu and Li 2016), Eurasian non-monsoon land
100 heating (Zhao et al. 2016), and North Pacific sea surface temperature (SST) anomaly
101 (Lau and Weng 2002; Lau et al. 2004), rather than the IPO and AMO. We aim to
102 address these shortcomings in this study.
103 The observed precipitation records are shorter than 150 years over the US and the
104 quality of the records decline significantly backward in time. In China, most of
105 meteorological stations were established after 1960s and only few stations were
106 available before 1960s, resulting in only about 60 stations with approximately 100
107 years of precipitation observations. These datasets are just enough to cover one (or two)
108 full cycles of the AMO and the IPO, which limits their utility for diagnosing robust

109 regional climate impacts linked with the IPO and AMO. For instance, Newman et al.
110 (2016) indicated that climate impacts correlated with the PDO are different from
111 climate impacts that are predicted by the PDO, because that climate impacts and the
112 PDO may be both driven by a common forcing function. It is difficult to distinguish
113 these two relationships in observation. Atmospheric general circulation models
114 (AGCMs) with prescribed observed or idealized SST patterns (e.g., Li et al. 2010; Hu et
115 al. 2011; Dai 2013; Schubert et al. 2009) are effective tools to confirm or reject
116 conclusions reached from observational analysis. Thus, in addition to observational and
117 reanalysis data, a series of AGCM experiments designed by the US Climate Variability
118 and Predictability (CLIVAR) Drought Working Group (Schubert et al. 2009) are also
119 employed in this study. As they are not fully coupled, there experiments are not suitable
120 to disentangle air-sea interaction. Detailed physical mechanisms of the interdecadal
121 oceanic modes and their potential influence to the seesaw relationship have not been
122 addressed in this study, and further follow-up work is needed.
123 The rest of the paper is organized as follows. In section 2, we describe the data,
124 AGCM experiments and methods used in this study. The observed seesaw pattern and
125 associated circulation are presented in section 3. The possible mechanisms are provided
126 in section 4. A summary and discussion are given in section 5.
127
128 **2. Data and methods**
129 ***a. Data***
130 The following datasets are used in this study.

1) Global merged monthly precipitation (based on gauge records) for 1850-2014 on a 2.5º latitude × 2.5º longitude grid obtained from Dai (2011; 2013). We focused on the period 1900-2014 because precipitation observations are sparse over China before around 1900.

2) Global land monthly precipitation for 1901-2015, with a high resolution of 0.5° latitude × 0.5° longitude, obtained from CRU TS4.0 (University of East Anglia Climatic Research Unit, 2017).

3) Chinese long-term gridded precipitation data for 1900-2009 obtained from the China Meteorological Administration.

4) Global atmospheric reanalysis monthly data for circulation for 1948-2016 on a 2.5º latitude × 2.5º longitude grid, from the U.S. National Centers for Environmental Prediction/National Center for Atmospheric Research (NCEP–NCAR; Kalnay et al. 1996).

5) Global gridded monthly SST for 1901-2016 on a 2º latitude × 2º longitude grid, from the National Oceanic and Atmospheric Administration Extended Reconstructed SST version 4 (ERSST v4; Huang et al. 2015).

6) The annual IPO index for 1920-2015, from Dai (2013), who defined the smoothed (by applying a 9-year moving average twice) associated principle component of the second leading empirical orthogonal function (EOF) of the 3-year moving averaged SST from the Hadley Centre Sea Ice and Sea Surface Temperature dataset (HadISST; Rayner et al. 2003), using data for 1920-2011 and 60ºS–60ºN.

7) The monthly AMO index for 1856-2016 (Enfield et al. 2001) downloaded from

https://www.esrl.noaa.gov/psd/data/timeseries/AMO/.

b. AGCM experiments

The US CLIVAR Drought Working Group initiated a series of global climate model experiments to address the physical mechanisms that link global SST variations to regional drought and flood (Schubert et al. 2009). Associated forcing SST fields for experiments were prescribed as follows.

1) The Rotated Empirical Orthogonal Function (REOF) method was applied to global annual-mean SST anomalies (Rayner et al. 2003) from 1901 to 2004 to obtain the leading patterns of SST anomalies.
2) The REOF2 (Fig. 1a) was scaled by ±2σ (σ is the standard deviation of the associated Rotated Principal Component (RPC2, Fig. 1b)) and then superimposed onto the 1901-2004 monthly climatology, forming a forcing SST anomaly called the Pacific pattern.
3) Applying the method in (2) to the REOF3 (Fig. 1c) yields the Atlantic pattern.

As shown in Fig. 1a, the Pacific pattern is analogous to the IPO-associated SST anomaly, and RPC2 is significantly correlated with the IPO index; thus, the Pacific pattern is deemed the IPO in this study. Likewise, the Atlantic pattern is deemed the AMO. Note that the prescribed SST fields vary monthly with the climatological (1901-2004) seasonal cycle, but have no inter-annual or longer-term variability.

We focused on nine baseline experiments, which are combinations of the Pacific (P) and Atlantic (A) patterns of cold (denoted by *c*; scaled by -2σ), neutral (*n*; zero

anomaly), and warm (*w*; scaled by +2σ) anomalies (denoted by PxAy shown in Table 1, here x, y=*c*, *n, w*). These baseline experiments were performed by five AGCMs: the NASA Seasonal-to-Interannual Prediction Project AGCM (NSIPP1, Bacmeister et al. 2000), the Global Forecast System AGCM (GFS, Campana and Caplan 2005), the Geophysical Fluid Dynamics Laboratory AGCM (GFDL, Delworth et al. 2006), the Community Atmospheric Model (CAM3.5, Chen et al. 2010), and the Community Climate Model (CCM3, Kiehl et al. 1998). All simulations ran for 50 years, except the GFS (35 years). Additional experiments (performed by only GFDL and NSIPP1) forced by the tropical SST component of the Pacific pattern (Fig. 1a, blue box) were also analyzed. For more information and an overview of the US CLIVAR Drought Working Group, please see Schubert et al. (2009).

c. Methods

We focused on interdecadal precipitation variations and used a 9-year moving average twice, which is equivalent to a 17-year low-pass filter with unequal weights, to remove short-term variations. Regression analysis and epoch composites were employed to depict the spatial patterns of anomalous SST and atmospheric circulation associated with the precipitation and the IPO. The threshold of ±0.5σ of the IPO index was used to define the IPO cold and warm phases. The long-term trend in global SST was removed by regressing the SST with the time series of global annual mean SST, while the long-term trend in other variables was removed using a linear least square fit. The Student's *t*-test (Wilks 2005) was used to test the difference of mean during

different composite periods, and detect the statistical significance of linear regression coefficients and Pearson correlation coefficients, after adjusting the degrees of freedom (in supplement). In addition, simulations from all five AGCMs were averaged to obtain an ensemble mean, which often reduces model uncertainties introduced by sub-grid scale parameterizations and produces signals closer to observations (Rowell 1998; Wang et al. 2005; Mo et al. 2009).

3. Interdecadal seesaw and associated circulations

Figure 2a shows detrended and smoothed regional average precipitation anomalies over North China and the Southwest US, as well as the IPO and AMO indices. Precipitation variations over North China are significantly negatively correlated with those over the Southwest US, with wet (dry) over North China aligning with dry (wet) over the Southwest US, implying an apparent interdecadal seesaw pattern.

Note that a significant positive correlation is found between Southwest US precipitation and the IPO index, with the maximum correlation ($r = 0.90$) at zero lag, implying they vary in phase. North China precipitation is significantly anti-correlated with the IPO index at zero lag, suggesting they vary out of phase. This means that the IPO may be associated with the interdecadal seesaw pattern, with the warm IPO phase aligned with below-normal precipitation over North China but above-normal precipitation over the Southwest US and the cold IPO phase aligned with wet over North China but dry over the Southwest US (Fig. 2b). It is also noted that the maximum

219 negative correlation ($r = -0.62$) occurs when the IPO leads North China precipitation
220 by about 8 years (Fig. S2 in supplement). The 8-year lagged anti-correlation could be
221 one reason why the PDO trend during 1971–2012 is nearly zero, however, there is a
222 significant decline in North China precipitation mentioned by Zhou et al. (2013).
223 Unlike the IPO, the AMO has an insignificant positive correlation with North
224 China precipitation at zero lag, implying the AMO's contemporaneous influence on
225 precipitation is smaller than the IPO's. The maximum positive correlation ($r = 0.85$) is
226 found when the AMO leads precipitation by about 15 years, or approximately
227 one-quarter of an AMO cycle. The AMO has a significant anti-correlation with
228 precipitation over the Southwest US, with maximum negative correlation ($r = -0.81$)
229 when the AMO leads precipitation by about 11 years. This implies that the AMO has
230 opposite effect on the interdecadal seesaw with respect to the IPO. Additionally, the
231 AMO can only strengthen (weaken) the magnitude of the IPO-induced precipitation
232 anomaly, when the AMO is out of phase (in phase) with the IPO (Fig. 2b), respectively.
233 We also performed the same analysis using the CRU TS4.0 precipitation data. The
234 results (Fig. S1 in supplement) are analogous to those shown in Fig. 2a using the Dai
235 precipitation data, indicating that the relationships are robust and not sensitive to the
236 choice of data.
237 Given that the IPO may play a dominant role in the interdecadal seesaw pattern,
238 the IPO phase composite anomalies of SST and precipitation over North China and the
239 Southwest US are shown in Fig. 3. During the first cold IPO phase (1947-1972),
240 precipitation shows a north-south dipole, with above-normal precipitation over North

241 China but below-normal precipitation over South China (Fig. 3a). Meanwhile, most of
242 the contiguous US receives below-normal precipitation except parts of the northwest
243 and southeast, where precipitation increases (Fig. 3b). During the warm IPO phase
244 (1977-1998), the spatial pattern of precipitation anomalies resembles that associated
245 with the first cold IPO phase, but with opposite sign. However, note that the two cold
246 IPO phases have distinct precipitation anomalies. For the recent cold phase
247 (2003-2014), above- and below-normal precipitation is expected over North China and
248 the Southwest US, respectively. However, precipitation decreases in both regions. A
249 comparison of the SST anomalies associated with the two cold IPO phases (Fig. 3c and
250 3i), shows opposite-signed SST anomalies, except in the North Pacific. This implies
251 that other interdecadal SST modes, e.g., AMO, may influence regional precipitation
252 anomalies; over North China, their influences tend to be comparable to that of the IPO,
253 but over the Southwest US they are relatively smaller. In addition, the 8-year lag
254 anti-correlation between precipitation over North China and the IPO for 1920-2014 is
255 similar to that for 1920-2000 (Fig. S3 in supplement), suggesting that the lag
256 anti-correlation is robust. Therefore, the 8 years' lag could be another reason for the
257 negative precipitation anomaly in North China during the recent IPO cold phase, which
258 has thus far existed for only approximately a quarter of a traditional IPO cycle.
259 To explore global large-scale atmospheric circulation anomalies associated with
260 increased precipitation over North China and the Southwest US, some key circulation
261 variables as well as SST were separately regressed onto the smoothed regional mean
262 precipitation anomalies over the two regions (Fig. 4).

Associated with increased precipitation over North China, the predominant SST feature is a basin-wide warming in the northern North Pacific and cooling in the tropical eastern Pacific (Fig. 4a), which resembles the IPO cold phase (Fig. 3c). There is an anomalously low sea-level pressure (SLP) over China and Mongolia, while an anomalously high SLP occupies the entire northern North Pacific. A positive height anomaly in the upper troposphere is also found over the northern North Pacific, suggesting the anomalous high pressure has an equivalent barotropic structure (Fig. 4c). It is associated with an anomalous anticyclone extending from west coast of North America to east coast of Asia. The lower-tropospheric circulation over East China features anomalous southwesterlies, indicating an enhanced EASM circulation. These circulation anomalies favor water vapor transport from the tropics and convergence into North China, associated with increased precipitation over North China but reduced precipitation over South China.

Compared with North China, increased precipitation over the Southwest US is associated with opposite-signed anomalies in SST and circulation. The spatial pattern of SST anomalies is analogous to the warm IPO phase (Fig. 3f). The northern North Pacific is also dominated by an equivalent barotropic structure, but it is an anomalous low. The associated anomalous cyclone induces anomalous southwesterlies and increased precipitation over the Southwest US (Fig. 4d). Meanwhile, anomalous northerlies are found over East China, implying a weakened EASM and reduced precipitation over North China.

4. Possible formation mechanism of the interdecadal seesaw

a. Impact of the IPO

Illustrated in Fig. 5 are multi-model ensemble mean anomalies of regional mean annual and seasonal precipitation responses in the eight AGCM experiments over North China and the Southwest US. In PwAn (the Pacific warm SST anomaly and Atlantic SST in neutral condition), below-normal precipitation occurs over North China, whereas the Southwest US receives above-normal precipitation, implying a seesaw pattern. The seesaw pattern reverses sign in PcAn. The AMO also contributes to the seesaw pattern, but has the opposite influence, with wet (dry) anomalies over North China and dry (wet) anomalies over the Southwest US associated with PnAw (PnAc). With respect to the annual-mean precipitation in PnAn, the IPO causes precipitation variations of approximately 6.4% and 39.8% of the mean over North China and the Southwest US, respectively, while the AMO only induces variations of approximately 4.1% and 13.5% of the mean. These results suggest that the IPO is the primary influence on the seesaw pattern; its modulation tends to be intensified when the AMO is in the opposite phase, but weakened when the AMO is in the same phase. Besides, note that the intermodel consensus is much stronger for the precipitation responses over the Southwest US than that over North China, implying that the linkage between the IPO (AMO) and precipitation variations is stronger over the Southwest US, whereas there are some uncertainties over North China.

Generally, the AGCMs in this study simulate well the observed contrasting precipitation variability between North China and the Southwest US, as well as the

307 dominant role of the IPO in driving this contrast. The precipitation response over the
308 Southwest US to the IPO is much larger than that over North China. This is consistent
309 with Dong and Dai (2015), which found a robust precipitation response over the
310 Southwest US for two cold IPO phases in a CanAM4 simulation forced by observed
311 SSTs from 1950 to 2009, whereas the precipitation response was inconsistent over
312 North China. Additionally, the similarity between the precipitation responses in the
313 annual and seasonal averages, especially over the Southwest US, may be related to
314 imposing the annual-mean IPO or AMO SST anomaly onto the monthly climatology
315 (Schubert et al. 2009).

316 To clarify the impact of the IPO on the seesaw, Fig. 6 shows the annual-mean
317 atmospheric circulation response to PwAn and PcAn. In PwAn, the predominant
318 feature of the SLP (Fig. 6a) and height responses at 500 hPa (Fig. 6c) is a negative
319 anomaly occupying the entire northern North Pacific, implying a deepened Aleutian
320 low. This is accompanied by a large-scale cyclonic anomaly extending from the west
321 coast of North America to northern China. Meanwhile, there is an anticyclonic anomaly
322 centered over the northwest Pacific. Combined, these circulations induce anomalous
323 northwesterlies over North China and southwesterlies over both the Southwest US and
324 South China, and a belt of anomalous moisture transport from the Bay of Bengal, South
325 China Sea and the subtropical Pacific to the west coast of North America (Fig. 6e). This
326 increased moisture transport is associated with a belt of increased precipitation,
327 including the Southwest US and South China (Fig. 6g). Less precipitation falls over
328 North China, related to the increase in moisture convergence over South China

329 associated with the weakened EASM (Yang et al. 2017). The simulated circulation
330 patterns resemble those related to increased precipitation over the Southwest US in
331 observations (Fig. 4b and 4d). In PcAn (right column in Fig. 6), the spatial patterns of
332 the circulation responses are analogous to those in PwAn but with opposite signs, as
333 well as those related to increased precipitation over North China in observations (Fig.
334 4a and 4c).

335 Both observations and simulations suggest the IPO-induced height anomaly over
336 the northern North Pacific is critical in driving the seesaw pattern, via opposing wind
337 and moisture anomalies on its eastern and western sides. Next, we consider the possible
338 mechanisms for this height anomaly.

339 In PwAn, warm SST anomalies over the equatorial central-eastern Pacific warm
340 the tropical troposphere through enhanced surface heat fluxes from the ocean to the
341 atmosphere (Fig. 7a). Meanwhile, a zonal belt of extensive cooling exists over
342 approximately 30^{o}N-60^{o}N, which may be associated with changes in the eddy-driven
343 mean meridional circulation (Seager et al. 2003). Then, the meridional temperature
344 gradient (MTG), computed as the temperature difference from south to north,
345 strengthens over the region 15^{o}N-45^{o}N, collocated with enhanced westerlies in the
346 upper troposphere via thermal wind balance. In the tropics and high latitudes, the
347 weakened MTG is associated with anomalous easterlies. Associated with these wind
348 anomalies is a dipole pattern of relative vorticity changes at 200 hPa over the North
349 Pacific, with a cyclone over the northern North Pacific and an anticyclone over the
350 southern North Pacific, with a dividing line at approximately 40^{o}N (Fig. 7c).

351 Consequently, an anomalous upper-troposphere low-pressure center forms over the
352 northern North Pacific.

353 On the other hand, the mean meridional circulation over the North Pacific changes
354 in response to the increased atmospheric heating over the tropical ocean. The thermally
355 direct Hadley cell is strengthened by enhanced tropical convection (Fig. 7g), itself due
356 to enhanced surface evaporation and low-level moisture convergence. The
357 strengthened descending motion in the subsiding branch of the Hadley cell, centered at
358 approximately 20^{o}N, aligns with an anomalous anticyclone at 850 hPa (Fig. 7e). In the
359 lower troposphere, the northward flow from the subtropical anomalous anticyclone
360 converges in the mid-latitudes and enhances the ascending branch of the Ferrel cell,
361 forming an anomalous cyclone over the northern North Pacific. Therefore, in PwAn, a
362 barotropic low-pressure anomaly extends across the northern North Pacific, which is
363 clearly related to the planetary-scale response of the atmosphere to the tropical warm
364 SST anomalies.

365 Collocated with vertical velocity anomalies (upward-downward-upward from
366 south to north, Fig. 7g) over the North Pacific, there is above-normal precipitation in
367 the tropics (10^{o}S-10^{o}N), below-normal precipitation in the subtropics (10^{o}N-30^{o}N), and
368 above-normal precipitation in the mid-latitudes (30^{o}N-50^{o}N, Fig. 7i). Note that the
369 above-normal precipitation overlies cold SST anomalies across the northern North
370 Pacific. The opposing signs of the precipitation and SST anomalies suggests that the
371 increased precipitation is forced remotely, not by local SST anomalies (Wu and
372 Kirtman 2007), strengthening the conclusion that the negative height anomaly over the

northern North Pacific is a response to the IPO-associated tropical warm SST anomalies via the atmospheric bridge.

Then, a question naturally arises: Do the tropical SST component of the IPO induce the height anomaly over the northern North Pacific? To answer the question, additional experiments (performed by only GFDL and NSIPP1) forced by the tropical SST component of the Pacific pattern were also analyzed and compared with the baseline experiments.

Overall, circulation responses in AGCMs forced by the tropical SST anomaly only (TP) support the above finding (Fig. 8). Like PwAn, TPwAn also induces a tripole pattern of temperature anomalies over the North Pacific (warm-cold-warm from south to north), which is associated with a tripole structure of zonal wind anomalies (easterlies-westerlies-easterlies), due to the MTG changes. These favor a dipole pattern of relative vorticity shear in the upper troposphere, with positive vorticity over the northern North Pacific and negative vorticity over south of it. The former is associated with a barotropic low-pressure anomaly, accompanied by a large-scale cyclonic flow over the northern North Pacific and adjacent regions in the lower troposphere. Consequently, the seesaw pattern forms (Fig. 9 and Fig. S5 in supplement), characterized by dry over North China and wet over the Southwest US.

The atmospheric processes associated with PcAn (right column in Fig. 7) and TPcAn (Fig. S4 in supplement) resemble those associated with PwAn and TPwAn, respectively, but with the opposite sign. A barotropic high-pressure anomaly extends across the northern North Pacific in response to the IPO-associated tropical cold SST

anomalies.

b. Impact of the AMO

Both observations (Fig. 2b) and simulations (Fig. 5) suggest that compared with the IPO, the AMO plays an opposite and secondary role in the contrasting precipitation variability between North China and the Southwest US. This finding is also supported by the height response over the northern North Pacific, which is a critical circulation system associated with the seesaw pattern. As clearly shown in Fig. 10, opposite pressure anomalies are associated to the IPO and AMO. In addition, the magnitude of the AMO-induced height anomaly is only approximately one-third to one-half that induced by the IPO, suggesting the IPO plays a dominant role. The IPO-induced height anomaly is intensified when the AMO in the opposite phase (PwAc and PcAw), whereas it is slightly weakened when the AMO in the same phase (PwAw and PcAc).

How does the AMO affect the IPO? It has been suggested that the impact of the AMO on the IPO could be through two pathways: 1) the mid-latitude atmosphere process, the AMO could modify the atmospheric anomalies over Eurasia and further the northern North Pacific via downstream energy propagation at the mid-high latitudes (e.g., Si and Ding, 2016); 2) the tropical atmosphere process, the AMO could generate a trans-basin SLP seesaw, characterized by opposite SLP trends in the Pacific and the Indo-Atlantic region, and further change SST over the eastern tropical Pacific via a modification of the Walker circulation involving low-level wind anomalies (e.g., McGregor et al. 2014). No matter through which pathways, the warm

417 (cold) AMO phase tends to induce the cold (warm) IPO phase. This is supported that
418 there exists a significant lag anti-correlation between the AMO and the IPO indices
419 with the AMO index leading by approximately 11~12 years (Wu et al. 2011; Chylek et
420 al. 2014).

421 In the CLIVAR AGCMs experiments, the AMO may affect the modulation of the
422 IPO on circulation and precipitation through the first pathway. PnAw (PnAc) drives an
423 eastward-propagating wave train over Eurasia and then, induces a barotropic high
424 (low)-pressure anomaly over the northern North Pacific (Fig. 6 in Yang et al. (2017);
425 also seen Fig. S6 in supplement), which is consistent with the height anomaly
426 associated to PcAn (PwAn). Consequently, circulation and precipitation responses to
427 PnAw (PnAc) closely resemble those associated with PcAn (PwAn), although with
428 smaller magnitude. When the AMO in combination with the IPO in the opposite phases,
429 PwAc and PcAw (Fig. S7 in supplement), precipitation and circulation responses
430 resemble those in PwAn and PcAn (Fig. 6), respectively, but the strengthened height
431 anomaly over the northern North Pacific is associated with larger anomalies of wind,
432 moisture flux and precipitation (Fig. 11 and Fig. S8 in supplement).

433

434 **5. Conclusions and discussion**

435 Using data from observations, reanalysis and a set of AGCMs simulations forced
436 by idealized IPO- and AMO-associated SST anomalies, we compared the interdecadal
437 precipitation variations over North China and the Southwest US, as well as the
438 associated circulations. Our main findings are summarized as follows:

Firstly, on interdecadal scales, precipitation variations over North China and the Southwest US are anti-correlated, implying a seesaw pattern. The IPO could play a dominant role in driving the seesaw pattern, with the warm IPO phase associated with less precipitation over North China but more over the Southwest US; the cold phase is associated with the opposite-signed pattern. The AMO contributes oppositely and less. The IPO-induced precipitation anomaly intensifies when the AMO is in the opposite phase, whereas it is slightly weakened when the AMO in the same phase. The IPO has a much stronger influence on precipitation variations over the Southwest US than that over North China. AGCM simulations from the US CLIVAR Drought Working Group capture these relationships well.

Secondly, for the IPO, the large-scale lower-tropospheric cyclonic or anticyclonic circulation anomaly across the northern North Pacific is the predominant factor in driving the seesaw pattern. During the warm IPO phase, North China and the Southwest US, which are located at the western and eastern parts of the deepened Aleutian low, experience anomalous northwesterlies and southwesterlies, and receive below-normal and above-normal precipitation, respectively. Opposite-signed circulation anomalies are associated with the cold IPO phase.

Thirdly, the height anomaly over the northern North Pacific, which exhibits an equivalent barotropic structure, is part of the planetary-scale atmospheric response to the IPO-associated tropical SST anomaly. For instance, the warm IPO phase induces a tripole pattern of temperature anomalies over the North Pacific (warm-cold-warm from south to north), that strengthens the mid-latitude meridional temperature gradient but

461 weakens it in the tropics and high latitudes. By thermal wind balance, these are
462 accompanied by a tripole structure of zonal wind anomaly
463 (easterlies-westerlies-easterlies) that favors a dipole pattern of upper-tropospheric
464 relative vorticity shear, with positive vorticity over the northern North Pacific and
465 negative vorticity to the south. Consequently, a barotropic cyclonic anomaly extends
466 across the northern North Pacific.

467 Given the association between IPO (AMO) phase and interdecadal precipitation
468 variations over North China and the Southwest US, improved prediction of the IPO
469 (AMO) could provide a potential predictability of drought-related water stresses over
470 the two regions, although there are still many uncertainties in our understanding and
471 prediction of these interdecadal oceanic modes. If the phase of the IPO turns positive,
472 as it is projected in late 2014 (Meehl et al. 2016), North China may experience
473 anomalously decreased precipitation, whereas precipitation may enhance across much
474 of North America, including the Southwest US. However, we caution that this analysis
475 considers the IPO and AMO only, and neglects other processes, for instance
476 anthropogenic greenhouse gases and aerosols, which may also induce interdecadal
477 precipitation variability, either through a direct effect on precipitation or an indirect
478 influence on the magnitude or period of the IPO and AMO (e.g., Dong et al. 2014;
479 Smith et al. 2016; Liguori and Di Lorenzo 2018).

480 The observed seesaw pattern is the result of air-sea interactions, although the SST
481 may play a more active role than the atmosphere. However, AGCM simulations used
482 in this study cannot reflect the feedback of the atmosphere to the SST, which may

lead to erroneous attribution conclusions for decadal-scale circulation and precipitation variability, especially in East Asia (Dong et al. 2017). Additionally, the AGCM simulations show only the steady-state response, which cannot distinguish which circulation feature occurs first in response to the tropical SST anomaly, and thus may cause uncertainty in the potential pathway described here. The Pacific SST forcing (Fig. 1a) used in the AGCM simulations includes a same-signed SST anomaly in the Indian Ocean, which has been shown to contribute to precipitation variations over the US (e.g., Hoerling and Kumer 2003) and North China. The role of the Indian Ocean in the anti-correlation of precipitation over North China and Southwest US is not clear. These issues require further investigation to verify the link between the interdecadal seesaw pattern and the IPO and AMO.

Acknowledgments This study is jointly sponsored by the National Key R&D Program of China (2016YFA0600404), the National Natural Science Foundation of China (41530532, 41705073), the China Special Fund for Meteorological Research in the Public Interest (GYHY201106028, GYHY201506001-1), and the Jiangsu Collaborative Innovation Center for Climate Change. Nicholas P. Klingaman was funded by an Independent Research Fellowship from the UK Natural Environment Research Council (NE/L010976/1). Peili Wu was supported by the UK-China Research and Innovation Partnership Fund through the Met Office Climate Science for Services Partnership (CSSP), as part of the Newton Fund.

505 **References**

506 Bacmeister, J., P. J. Pegion, S. D. Schubert, and M. J. Suarez, 2000: *An Atlas of*
507 *Seasonal Means Simulated by the NSIPP 1 Atmospheric GCM*. NASA Tech.
508 Memo. 104606, Vol. 17, Goddard Space Flight Center, 194 pp.

509 Campana, K., and P. Caplan, Eds., 2005: *Technical procedure bulletin for the T382*
510 *Global Forecast System*. NOAA/NCEP/EMC.

511 Chen, H., T. Zhou, R. B. Neale, X. Wu and G. J. Zhang, 2010: Performance of the New
512 NCAR CAM3.5 in East Asian Summer Monsoon Simulations: Sensitivity to
513 Modifications of the Convection Scheme. *J. Climate*, **23**, 3657-3675, doi:
514 10.1175/2010JCLI3022.1.

515 Chylek, P., M. K. Dubey, G. Lesins, J. N. Li and N. Hengartner. 2014: Imprint of the
516 Atlantic multi-decadal oscillation and Pacific decadal oscillation on southwestern
517 US climate: past, present, and future. *Climate Dynamics*, **43**, 119-129.

518 Dai, A., 2011: Characteristics and trends in various forms of the Palmer Drought
519 Severity Index during 1900–2008. *J. Geophys. Res*. **116**, D12115.

520 Dai, A., 2013: The influence of the inter-decadal Pacific oscillation on US precipitation
521 during 1923-2010. *Clim. Dyn*., **41**, 633-646, doi:10.1007/s00382-012-1446-5.

522 Delworth, T. L., and Coauthors, 2006: GFDL's CM2 global coupled climate models.
523 Part I: Formulation and simulation characteristics. *J. Climate*, **19**, 643-674,
524 doi:10.1175/JCLI3629.1.

525 Di Lorenzo, E., G. Liguori, N. Schneider, J. C. Furtado, B. T. Anderson, and M. A.
526 Alexander, 2015: ENSO and meridional modes: A null hypothesis for Pacific

climate variability. *Geophysical Research Letters*, **42,** 9440-9448.

Dong, B., and A. Dai, 2015: The influence of the Interdecadal Pacific Oscillation on Temperature and Precipitation over the Globe. *Climate Dynamics*, **45,** 2667-2681.

Dong, B., Sutton, R.T., Shaffrey, L. and Klingaman, N. P., 2017: Attribution of Forced Decadal Climate Change in Coupled and Uncoupled Ocean–Atmosphere Model Experiments. *J. Climate*, **30** 6203-6223.

Dong, L., T. Zhou, and X. Chen, 2014: Changes of Pacific decadal variability in the twentieth century driven by internal variability, greenhouse gases, and aerosols. *Geophysical Research Letters*, **41,** 8570-8577.

Enfield, D. B., A. M. Mestas-Nunez, and P. J. Trimble, 2001: The Atlantic Multidecadal Oscillation and its relationship to precipitation and river flows in the continental U.S. *Geophys. Res. Lett.*, **28**: 2077-2080.

Fang, K., D. Chen, J. Li, and H. Seppä, 2014: Covarying Hydroclimate Patterns between Monsoonal Asia and North America over the Past 600 Years. *Journal of Climate*, 27, 8017-8033.

Fang, K., H. Seppä, and D. Chen, 2015: Interdecadal hydroclimate teleconnections between Asia and North America over the past 600 years. *Climate Dynamics*, 44, 1777-1787.

Farneti, R., F. Molteni, and F. Kucharski, 2014: Pacific interdecadal variability driven by tropical-extratropical interactions. *Climate Dynamics*, **42,** 3337-3355.

Feng, S., Q. Hu and R. J. Oglesby, 2011: Influence of Atlantic sea surface temperatures on persistent drought in North America. *Climate Dyn.*, **37**, 569-586,

549 doi:10.1007/s00382-010-0835-x.
550 Henley, B. J., 2017: Pacific decadal climate variability: Indices, patterns and
551 tropical-extratropical interactions. *Global and Planetary Change*, **155,** 42-55.
552 Henley, B. J., and Coauthors, 2017: Spatial and temporal agreement in climate model
553 simulations of the Interdecadal Pacific Oscillation. *Environmental Research*
554 *Letters*, **12**.
555 Hoerling, M. and Kumar, A., 2003: The perfect ocean for drought. *Science*, **299**, 691-4.
556 Hua, L., Z. Ma and L. Zhong, 2011: A comparative analysis of primary and extreme
557 characteristics of dry or wet status between Asia and North America. *Adv. Atmos.*
558 *Sci*., **28**, 352–362.
559 Huang, B., and Coauthors, 2015: Extended Reconstructed Sea Surface Temperature
560 Version 4 (ERSST.v4). Part I: Upgrades and Intercomparisons. *Journal of Climate*,
561 **28**, 911-930.
562 Huang, J., and Coauthors, 2017: Dryland climate change: Recent progress and
563 challenges. *Reviews of Geophysics*, **55,** 719-778.
564 Hu, Q., S. Feng, and R. J. Oglesby, 2011: Variations in North American Summer
565 Precipitation Driven by the Atlantic Multidecadal Oscillation. *J. Climate*, **24**,
566 5555-5570.
567 Kalnay, E., and Coauthors, 1996: The NCEP/NCAR 40-Year Reanalysis Project. Bull.
568 Amer. Meteor. Soc., 77, 437–471,
569 doi:10.1175/1520-0477(1996)077,0437:TNYRP.2.0.CO;2.
570 Kang, S., and E. A. B. Eltahir, 2018: North China Plain threatened by deadly

heatwaves due to climate change and irrigation. *Nat Commun*, **9,** 2894.

Kerr, R. A., 2000: A north Atlantic climate pacemaker for the centuries. *Science*, **288**, 1984-1986. doi:10.1126/science.288.5473.1984.

Kiehl, J. T., J. J. Hack, G. B. Bonan, B. A. Boville, D. L. Williamson and P. J. Rasch, 1998: The National Center for Atmospheric Research Community Climate Model: CCM3. *J. Climate*, **11**, 1131-1149, doi:10.1175/1520-0442(1998)011<1131:TNCFAR>2.0.CO;2.

Lau, K., and H. Weng, 2002: Recurrent teleconnection patterns linking summertime precipitation variability over East Asia and North America. *Journal of the Meteorological Society of Japan*, **80,** 1309-1324.

Lau, K., J. Lee, K. Kim, and I. Kang, 2004: The North Pacific as a Regulator of Summertime Climate over Eurasia and North America. *Journal of Climate*, **17,** 819-833.

Li, H., A. Dai, T. Zhou and J. Lu, 2010: Responses of East Asian summer monsoon to historical SST and atmospheric forcing during 1950-2000. *Climate Dyn.*, **34**, 501-514, doi: 10.1007/s00382-008-0482-7.

Li, Q., S. Yang, V. E. Kousky, R. W. Higgins, K. M. Lau, and P. Xie, 2005: Features of cross-Pacific climate shown in the variability of China and US precipitation. *International Journal of Climatology*, 25, 1675-1696.

Li, S., and G. T. Bates, 2007: Influence of the Atlantic multidecadal oscillation on the winter climate of East China. *Adv. Atmos. Sci.*, **24**, 126–135, doi:10.1007/s00376-007-0126-6.

593 Liguori, G., and E. Di Lorenzo, 2018: Meridional Modes and Increasing Pacific
594 Decadal Variability Under Anthropogenic Forcing. *Geophysical Research*
595 *Letters*, **45,** 983-991.
596 Lu, R., B. Dong, and H. Ding, 2006: Impact of the Atlantic Multidecadal Oscillation on
597 the Asian summer monsoon. *Geophysical Research Letters*, **33**, L24701.
598 Ma, Z., 2007: The interdecadal trend and shift of dry/wet over the central part of North
599 China and their relationship to the Pacific Decadal Oscillation (PDO). *Chin. Sci.*
600 *Bull.*, **52**, 2130-2139, doi: 10.1007/s11434-007-0284-z.
601 Ma, Z. and C. Fu, 2007: Evidences of Drying Trend in the Global During the later Half
602 of 20th Century and Their Relationship with Large-Scale Climate Background.
603 *Sci. China Ser. D-Earth Sci.*, **50**, 776-788.
604 Ma, Z. and L. Shao, 2006: Relationship Between Dry/Wet Variation and the Pacific
605 Decade Oscillation (PDO) in Northern China During the Last 100 Years. *Chinese*
606 *Journal of Atmospheric Sciences*, **30**, 464-474. (in Chinese)
607 McCabe, G. J., M. A. Palecki, and J. L. Betancourt, 2004: Pacific and Atlantic Ocean
608 influences on multidecadal drought frequency in the United States. *Proc Natl*
609 *Acad Sci USA*, **101**, 4136-4141.
610 McGregor, S., A. Timmermann, M. F. Stuecker, M. H. England, M. Merrifield, F.-F.
611 Jin, and Y. Chikamoto, 2014: Recent Walker circulation strengthening and Pacific
612 cooling amplified by Atlantic warming. *Nature Climate Change*, **4,** 888-892.
613 Mantua, N. J., S. R. Hare, Y. Zhang, J. M. Wallace and R. C. Francis, 1997: A Pacific
614 interdecadal climate oscillation with impacts on salmon production. *Bull. Amer.*

615 *Meteor. Soc.*, **78**, 1069-1079,
616 doi:10.1175/1520-0477(1997)078<1069:APICOW>2.0.CO;2.
617 Mantua, N. J. and S. R. Hare, 2002: The Pacific decadal oscillation. *J. Oceanogr.*, **58**,
618 35-44, doi: 10.1023/A:1015820616384.
619 Meehl, G. A., and A. Hu, 2006: Megadroughts in the Indian Monsoon Region and
620 Southwest North America and a Mechanism for Associated Multidecadal Pacific
621 Sea Surface Temperature Anomalies. *J. Climate*, **19**, 1605-1623.
622 Meehl, G. A., A. Hu, and H. Teng, 2016: Initialized decadal prediction for transition to
623 positive phase of the Interdecadal Pacific Oscillation. *Nat Commun*, **7,** 11718.
624 Mo, K. C., J.-K. E. Schemm and S.-H. Yoo, 2009: Influence of ENSO and the Atlantic
625 Multidecadal Oscillation on Drought over the United States. *J. Climate*, **22**,
626 5962-5982, doi:10.1175/2009JCLI2966.1.
627 Newman, M., and Coauthors, 2016: The Pacific Decadal Oscillation, Revisited.
628 *Journal of Climate*, **29,** 4399-4427.
629 Power, S., T. Casey, C. Folland, A. Colman, and V. Mehta, 1999: Inter-decadal
630 modulation of the impact of ENSO on Australia. *Climate Dyn.*, **15**, 319-324, doi:
631 10.1007/s003820050284.
632 Qian, C. and T. Zhou, 2014: Multidecadal Variability of North China Aridity and Its
633 Relationship to PDO during 1900–2010. *J. Climate*, **27**, 1210-1222,
634 doi:10.1175/JCLI-D-13-00235.1.
635 Rayner, N. A., D. E. Parker, E. B. Horton, C. K. Folland, L. V. Alexander, D. P. Rowell,
636 E. C. Kent and A. Kaplan, 2003: Global analyses of sea surface temperature, sea

637 ice, and night marine air temperature since the late nineteenth century. *J. Geophys.*
638 *Res. Atmos.*, **108**, 4407, doi:10.1029/2002JD002670.
639 Rowell, D. P., 1998: Assessing potential seasonal predictability with an ensemble of
640 multidecadal GCM simulations. *J. Climate*, **11**, 109-120,
641 doi:10.1175/1520-0442(1998)011<0109:APSPWA>2.0.CO;2.
642 Schubert, S., et al., 2009: A US CLIVAR Project to Assess and Compare the Responses
643 of Global Climate Models to Drought-Related SST Forcing Patterns: Overview
644 and Results. *J. Climate*, **22**, 5251-5272, doi:10.1175/2009JCLI3060.1.
645 Seager, R., Harnik, N. and Kushnir, Y., 2003: Mechanisms of Hemispherically
646 Symmetric Climate Variability. *J. Climate*, **16**, 2960-2978, doi:
647 10.1175/1520-0442(2003)016<2960:MOHSCV>2.0.CO;2.
648 Si, D., and Y. Ding, 2016: Oceanic forcings of the interdecadal variability in East Asian
649 summer rainfall. *J. Climate*, 29, 7633–7649, doi:10.1175/JCLI-D-15-0792.1.
650 Si, D., and A. Hu, 2017: Internally Generated and Externally Forced Multidecadal
651 Oceanic Modes and Their Influence on the Summer Rainfall over East Asia.
652 *Journal of Climate*, **30,** 8299-8316.
653 Smith, D. M., and Coauthors, 2016: Role of volcanic and anthropogenic aerosols in
654 the recent global surface warming slowdown. *Nature Climate Change*, **6,**
655 936-940.
656 Sutton, R. T., and D. L. Hodson, 2005: Atlantic Ocean forcing of North American and
657 European summer climate. *Science*, **309**, 115-118.
658 Sutton, R. T., and D. L. Hodson, 2007: Climate Response to Basin-Scale Warming and

659 Cooling of the North Atlantic Ocean. *J. Climate*, **20**, 891-907.
660 University of East Anglia Climatic Research Unit, I. C. Harris, P. D. Jones, 2017: CRU
661 TS4.00: Climatic Research Unit (CRU) Time-Series (TS) version 4.00 of high
662 resolution gridded data of month-by-month variation in climate (Jan. 1901- Dec.
663 2015). Centre for Environmental Data Analysis, 25 August 2017,
664 doi:10.5285/edf8febfdaad48abb2cbaf7d7e846a86.
665 Vellinga, M. and P. Wu, 2004: Low-latitude freshwater influence on centennial
666 variability of the thermohaline circulation. *J. Climate*, **17**, 4498-4511.
667 Wang, B., Q. H. Ding, X. H. Fu, I. S. Kang, K. Jin, J. Shukla and F. Doblas-Reyes, 2005:
668 Fundamental challenge in simulation and prediction of summer monsoon
669 precipitation. *Geophys. Res. Lett.*, **32**, L15711, doi:10.1029/2005GL022734.
670 Wang, F., S. Yang, W. Higgins, Q. Li, and Z. Zuo, 2014: Long-term changes in total
671 and extreme precipitation over China and the United States and their links to
672 oceanic-atmospheric features. *International Journal of Climatology*, 34, 286-302.
673 Wu, P., N. Christidis and P. Stott, 2013: Anthropogenic impact on Earth's hydrological
674 cycle. *Nature Climate Change*, **3**, 807-810.
675 Wu, P., J. Ridley, A. Pardaens, R. Leavine and J. Lowe, 2015: The reversibility of CO2
676 induced climate change. *Clim. Dyn.*, **45**, pp745-754.
677 Wu, R. and Kirtman, B.P., 2007. Regimes of seasonal air–sea interaction and
678 implications for performance of forced simulations. *Climate Dynamics*, **29**,
679 393-410.
680 Wu, S., Z. Liu, R. Zhang, and T. L. Delworth, 2011: On the observed relationship

between the Pacific Decadal Oscillation and the Atlantic Multi-decadal Oscillation. *Journal of Oceanography*, **67,** 27-35.

Wilks, D.S., 2005: Statistical methods in the atmospheric sciences: second edition. *International Geophysics Series*, 138:140.

Yang, L., and Z. Fu, 2016: Out-phased decadal precipitation regime shift in China and the United States. *Theoretical and Applied Climatology*, 130, 535-544.

Yang, Q., Z. Ma, and B. Xu, 2016: Modulation of monthly precipitation patterns over East China by the Pacific Decadal Oscillation. *Climatic Change*, **144,** 405-417.

Yang, Q., Z. Ma, X. Fan, Z.-L. Yang, Z. Xu, and P. Wu, 2017: Decadal Modulation of Precipitation Patterns over Eastern China by Sea Surface Temperature Anomalies. *Journal of Climate*, **30,** 7017-7033.

Zhang, L., P. Wu, T. Zhou 2017: Aerosol Forcing of Extreme Summer Drought over North China. *Environ. Res. Lett.*, **12**,034020.

Zhang, Y., J. M. Wallace, and D. S. Battisti, 1997: ENSO-like interdecadal variability: 1900–93. J. Climate, 10, 1004–1020, doi:10.1175/1520-0442(1997)010,1004:ELIV.2.0.CO;2.

Zhao, P., S. Yang, H. Wang, and Q. Zhang, 2011: Interdecadal Relationships between the Asian–Pacific Oscillation and Summer Climate Anomalies over Asia, North Pacific, and North America during a Recent 100 Years. *Journal of Climate*, **24**, 4793-4799.

Zhao, P., and Coauthors, 2016: Summer precipitation anomalies in Asia and North America induced by Eurasian non-monsoon land heating versus ENSO. *Sci Rep*, **6,** 21346.

Zhou, T., F. Song, R. Lin, X. Chen and X. Chen, 2013: The 2012 North China floods: explaining an extreme precipitation event in the context of a longer-term drying tendency [in "Explaining Extreme Events of 2012 from a Climate Perspective"]. *Bull. Amer. Meteor. Soc.*, **94**, S49-S51, doi:10.1175/BAMS-D-13-00085.1.

Zhu, Y., H. Wang, W. Zhou and J. Ma, 2011: Recent changes in the summer precipitation pattern in East China and the background circulation. *Climate Dyn.*, **36**, 1463-1473, doi: 10.1007/s00382-010-0852-9.

Zhu, Y., H. Wang, J. Ma, T. Wang, and J. Sun, 2015: Contribution of the phase transition of Pacific Decadal Oscillation to the late 1990s' shift in East China summer precipitation. *Journal of Geophysical Research: Atmospheres*, **120**, 8817-8827.

Zhu, Y., T. Wang and J. Ma, 2016: Influence of internal decadal variability on the summer precipitation in Eastern China as simulated by CCSM4. *Adv. Atmos. Sci.*, **33**, 706-714, doi: 10.1007/s00376-016-5269-x.

Zhu, Z., and T. Li, 2016: A New Paradigm for Continental U.S. Summer Rainfall Variability: Asia–North America Teleconnection. *Journal of Climate*, **29,** 7313-7327.

Table Caption List

Table 1. The combinations of Pacific and Atlantic SST anomaly patterns used to force the AGCMs. Here *w* refers to the warm phase of the pattern (scaled by +2σ), *n* denotes neutral (zero anomaly), and *c* refers to the cold phase (scaled by -2σ). The *PnAn* experiment denotes the control run forced with the annually varying climatological SST (Schubert et al. 2009).

Figure Caption List

Fig. 1 The second and third leading REOFs (ºC) and associated time-series RPCs (ºC) of annual mean SST from 1901 to 2004 (Schubert et al. 2009). (a) The Pacific ENSO-like SSTA pattern of REOF2 and (b) associated RPC2 and the IPO index. (c) The Atlantic AMO SSTA pattern of REOF3 and (d) associated RPC3 and AMO index. The blue curves (b and d) are smoothed time series obtained by applying a 9-year moving average twice to the bars to emphasize the interdecadal variations. The same method is applied to the IPO and AMO indices. *r* and *p* represent the correlation coeffients between red and blue curves, and the statistical significance level, respectively. The percentages indicate the corresponding explained variances.

Fig. 2 (a) Detrended monthly precipitation anomalies over North China (110 ºE~118ºE, 34 ºN~42.5ºN) and the Southwest US (105 ºW~120ºW, 30 ºN~40ºN) and the IPO and AMO indices, obtained by applying a 109-month moving average twice. Observed precipitation anomalies over North China are referred to as “North China_station”.

Black dotted lines represent ±0.5σ of the IPO index. (b) Annual mean precipitation anomaly percentage (%) over North China and the Southwest US during different periods: cold IPO (IPO-), cold IPO plus warm AMO (IPO-AMO+), cold IPO plus cold AMO (IPO-AMO-), warm IPO (IPO+), warm IPO plus cold AMO (IPO+AMO-), and warm IPO plus warm AMO (IPO+AMO+), with respect to the climatology from 1920 to 2014. Statistically significant anomalies at the 5% level are indicated by black triangles.

Fig. 3 The IPO phase composite anomaly (relative to 1900-2014) maps of the detrended precipitation (mm day^{-1}) over North China (left column) and the Southwest US (middle column), and annual mean SST (ºC, right column) for the cold (a, b, and c, 1947-1972; g, h, and i, 2003-2014) and warm epoches (d, e, and f, 1977-1998), respectively. The boundaries of North China and the Southwest US are outlined in blue boxes. The dotted areas represent statistically significant anomalies at the 5% level.

Fig. 4 Regression maps of the detrended monthly (a) (b) SST (ºC, shaded) and SLP (hPa, contours), (c) (d) 200 hPa geopotential height (Z, m, contours) and 850 hPa wind (UV, m s^{-1}, vector) regressed onto the detrended monthly precipitation anomalies over North China and the Southwest US. The SST, circulation variables and precipitation are smoothed by applying a 109-month moving average twice. Only statistically significant (p<0.05) regression coefficients of 850 hPa wind are illustrated. The dotted and shaded areas represent significant (p<0.05) regression coefficients of

SST and 200 hPa geopotential height, repectively.

Fig. 5 Multi-model ensemble mean anomalies of annual and seasonal precipitation (mm day^{-1}) over (a) North China and (b) the Southwest US relative to the control run (PnAn). Error bars indicate the intermodel range. Here, P and A denote the Pacific (IPO) and Atlantic (AMO) SST anomaly patterns; *w*, *n* and *c* refer to the warm, neutral and cold phases, respectively (Table 1).

Fig. 6 Multi-model ensemble mean anomalies of annual mean (a) (b) SLP (hPa, shaded) and its climatology in PnAn (hPa, contours); (c) (d) 500-hPa geopotential height (Z, m, shaded) and 850 hPa wind (UV, m s^{-1}, vectors); (e) (f) column-integrated moisture divergence (mm day^{-1}, shaded) and moisture flux (g cm^{-1} s^{-1}, vectors); (g) (h) precipitation (Pre, mm day^{-1}, shaded), for PwAn (left column) and PcAn (right column). Note that an unequal contour interval is used to highlight the response over land. Stippling indicates areas where more than four of the five AGCMs agree on the sign.

Fig. 7 Multi-model ensemble mean anomalies of annual mean (a) (b) air temperature (T, from surface to 200 hPa, contours, K) and 200 hPa zonal wind (U, shaded, m s^{-1}); wind (UV, m s^{-1}, vectors) and relative vorticity (scaled by 1e5, s^{-1}, shaded) at (c) (d) 200 hPa, and (e) (f) 850 hPa; (g) (h) meridional (V, m s^{-1}, vectors) and vertical (W, 10^{-3} m s^{-1}, shaded) circulation, and (i) (j) SST (scaled by 2, ^{o}C) and precipitation (Pre, mm day^{-1}) over the Pacific (average 150^{o}E~120^{o}W), for PwAn (left column) and PcAn (right

column). For convenience in comparing quantitatively the precipitation responses in different experiments, the zonal-mean precipitation anomalies in experiments with the warm (Pw) and cold IPO (Pc), as well as PnAc and PnAw, are illustrated in (i) and (j), respectively.

Fig. 8 Anomalies of annual mean (a) (b) air temperature (T, from surface to 200 hPa, contours, K) and 200 hPa zonal wind (U, shaded, m s^{-1}); wind (UV, m s^{-1}, vectors) and relative vorticity (scaled by 1e5, s^{-1}, shaded) at (c) (d) 200 hPa, and (e) (f) 850 hPa for TPwAn in GFDL (left column) and NSIPP1 (right column).

Fig. 9 Responses of annual mean precipitation (mm day^{-1}, shaded) to the Pacific pattern (PwAn and PcAn) and its tropical SST component (TPwAn and TPcAn) in GFDL. The dotted areas represent statistically significant anomalies at the 5% level.

Fig. 10 Multi-model ensemble mean anomalies of annual mean geopotential height (m) over the northern North Pacific (30°-65°N, 160°E-140°W) from surface to 70 hPa.

Fig. 11 Left column: Multi-model ensemble mean differences between PwAc and PwAn: (a) SLP (hPa, shaded) and SLP climatology in PwAn (hPa, contours); (c) 500 hPa geopotential height (Z, m, shaded) and 850 hPa wind (UV, m s^{-1}, vectors); (e) column-integrated moisture divergence (mm day^{-1}, shaded) and moisture flux (g cm^{-1} s^{-1}, vectors); (g) precipitation (Pre, mm day^{-1}, shaded). Right column is the same as left

89 one, but for differences between PcAw and PcAn.

90

91 **Tables**

92 **Table 1.** The combinations of Pacific and Atlantic SST anomaly patterns used to force
93 the AGCMs. Here *w* refers to the warm phase of the pattern (scaled by +2σ), *n* denotes
94 neutral (zero anomaly), and *c* refers to the cold phase (scaled by -2σ). The *PnAn*
95 experiment denotes the control run forced with the annually varying climatological
96 SST (Schubert et al. 2009).

	Warm Atlantic	Neutral Atlantic	Cold Atlantic
Warm Pacific	PwAw	PwAn	PwAc
Neutral Pacific	PnAw	PnAn	PnAc
Cold Pacific	PcAw	PcAn	PcAc
Warm tropical Pacific	-	TPwAn	-
Cold tropical Pacific	-	TPcAn	-

97

Figures

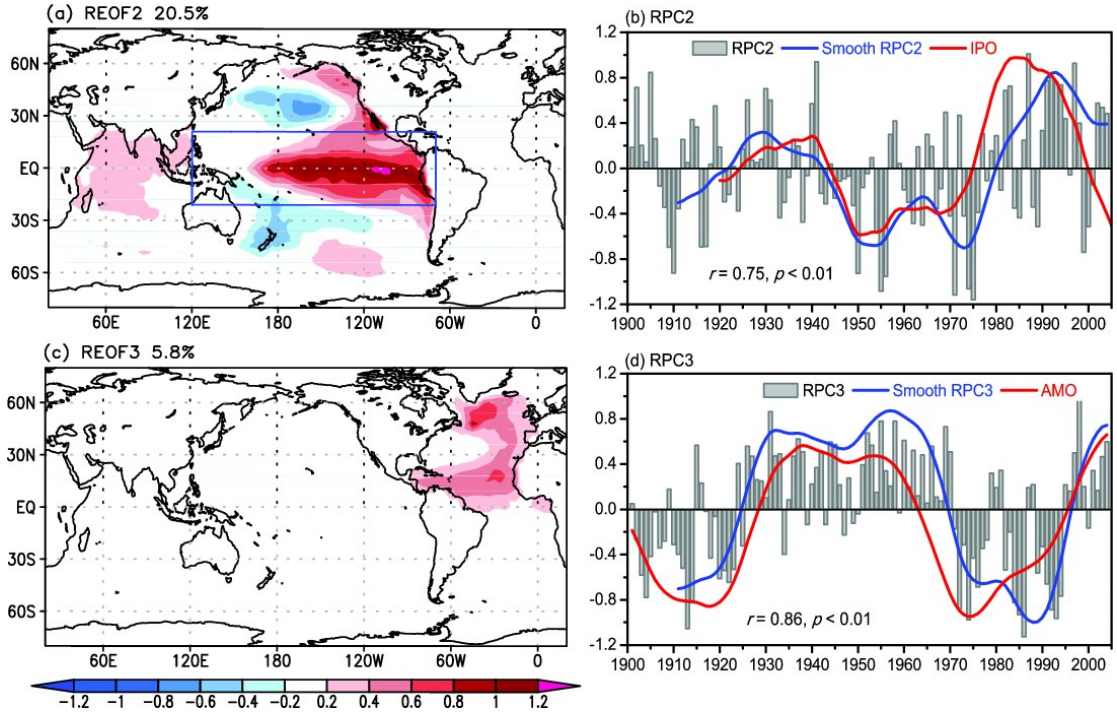

Fig. 1 The second and third leading REOFs (ºC) and associated time-series RPCs (ºC) of annual mean SST from 1901 to 2004 (Schubert et al. 2009). (a) The Pacific ENSO-like SSTA pattern of REOF2 and (b) associated RPC2 and the IPO index. (c) The Atlantic AMO SSTA pattern of REOF3 and (d) associated RPC3 and AMO index. The blue curves (b and d) are smoothed time series obtained by applying a 9-year moving average twice to the bars to emphasize the interdecadal variations. The same method is applied to the IPO and AMO indices. *r* and *p* represent the correlation coeffients between red and blue curves, and the statistical significance level, respectively. The percentages indicate the corresponding explained variances.

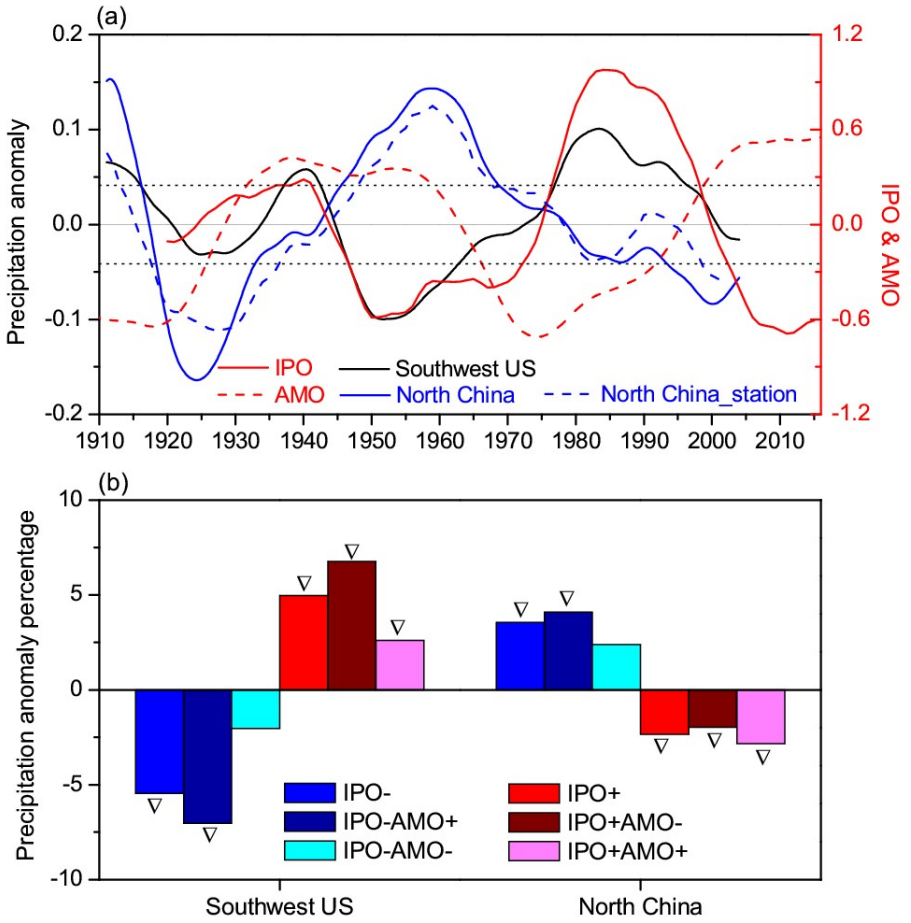

Fig. 2 (a) Detrended monthly precipitation anomalies over North China (110 ºE~118ºE, 34 ºN~42.5ºN) and the Southwest US (105 ºW~120ºW, 30 ºN~40ºN) and the IPO and AMO indices, obtained by applying a 109-month moving average twice. Observed precipitation anomalies over North China are referred to as "North China_station". Black dotted lines represent ±0.5σ of the IPO index. (b) Annual mean precipitation anomaly percentage (%) over North China and the Southwest US during different periods: cold IPO (IPO-), cold IPO plus warm AMO (IPO-AMO+), cold IPO plus cold AMO (IPO-AMO-), warm IPO (IPO+), warm IPO plus cold AMO (IPO+AMO-), and warm IPO plus warm AMO (IPO+AMO+), with respect to the climatology from 1920 to 2014. Statistically significant anomalies at the 5% level are indicated by black triangles.

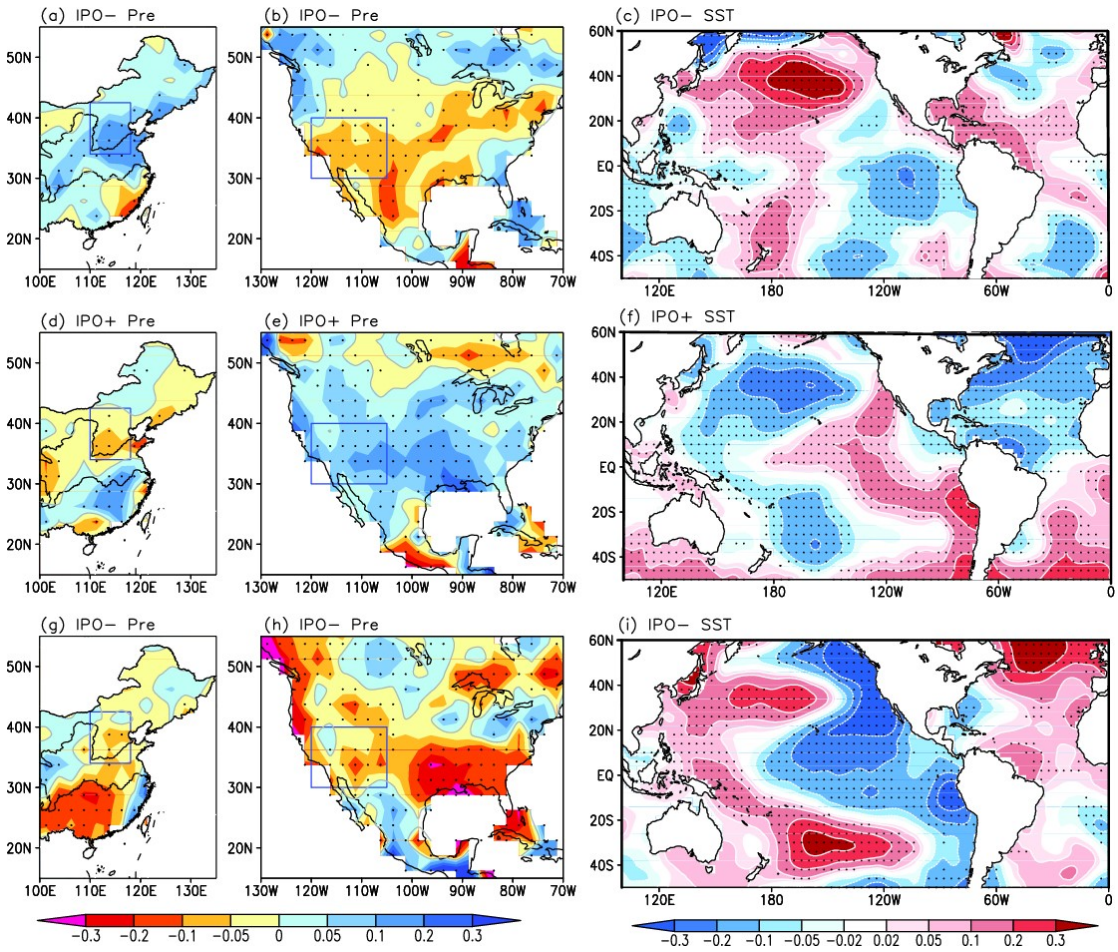

Fig. 3 The IPO phase composite anomaly (relative to 1900-2014) maps of the detrended precipitation (mm day^{-1}) over North China (left column) and the Southwest US (middle column), and annual mean SST (^{o}C, right column) for the cold (a, b, and c, 1947-1972; g, h, and i, 2003-2014) and warm epoches (d, e, and f, 1977-1998), respectively. The boundaries of North China and the Southwest US are outlined in blue boxes. The dotted areas represent statistically significant anomalies at the 5% level.

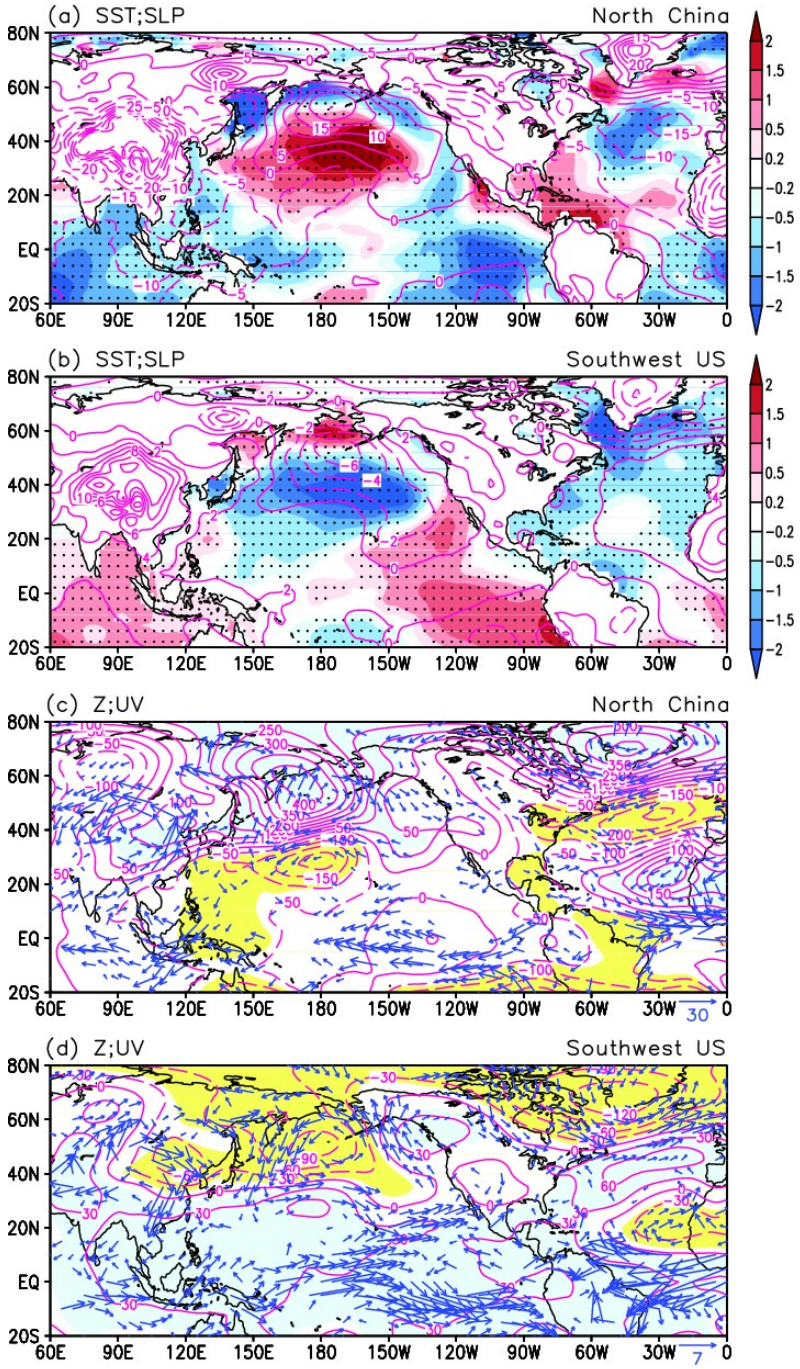

131

132 **Fig. 4** Regression maps of the detrended monthly (a) (b) SST (ºC, shaded) and SLP
133 (hPa, contours), (c) (d) 200 hPa geopotential height (Z, m, contours) and 850 hPa
134 wind (UV, m s^{-1}, vector) regressed onto the detrended monthly precipitation anomalies
135 over North China and the Southwest US. The SST, circulation variables and
136 precipitation are smoothed by applying a 109-month moving average twice. Only
137 statistically significant (p<0.05) regression coefficients of 850 hPa wind are illustrated.
138 The dotted and shaded areas represent significant (p<0.05) regression coefficients of
139 SST and 200 hPa geopotential height, repectively.

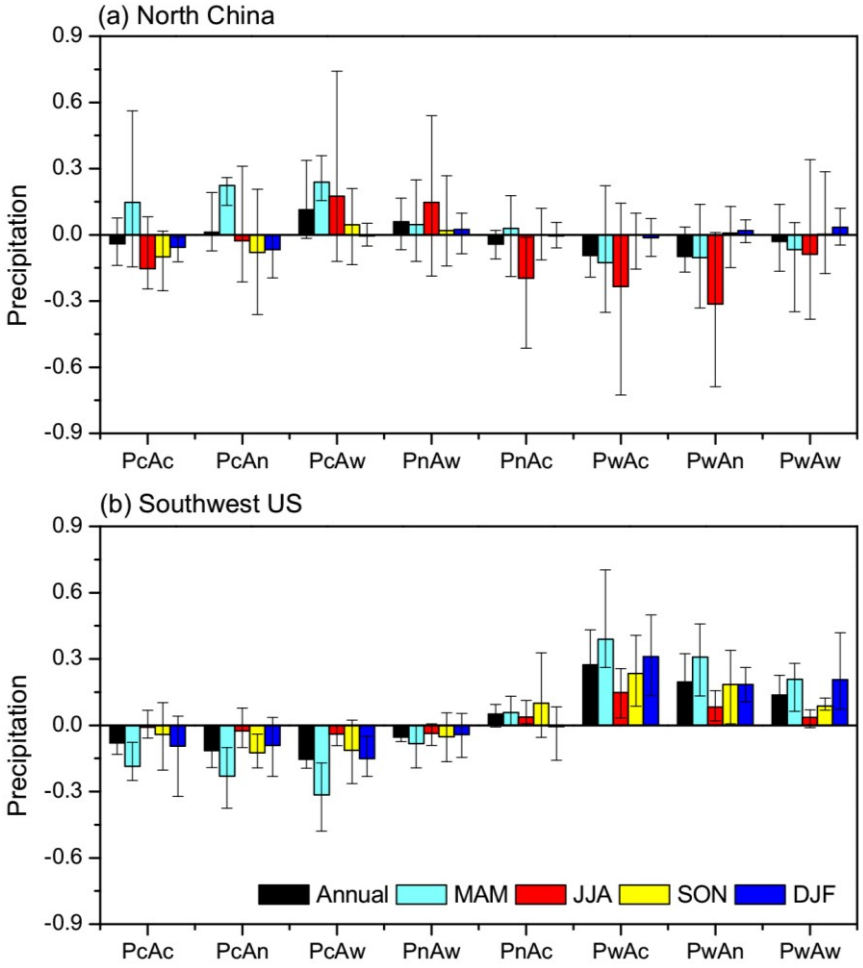

Fig. 5 Multi-model ensemble mean anomalies of annual and seasonal precipitation (mm day^{-1}) over (a) North China and (b) the Southwest US relative to the control run (PnAn). Error bars indicate the intermodel range. Here, P and A denote the Pacific (IPO) and Atlantic (AMO) SST anomaly patterns; *w*, *n* and *c* refer to the warm, neutral and cold phases, respectively (Table 1).

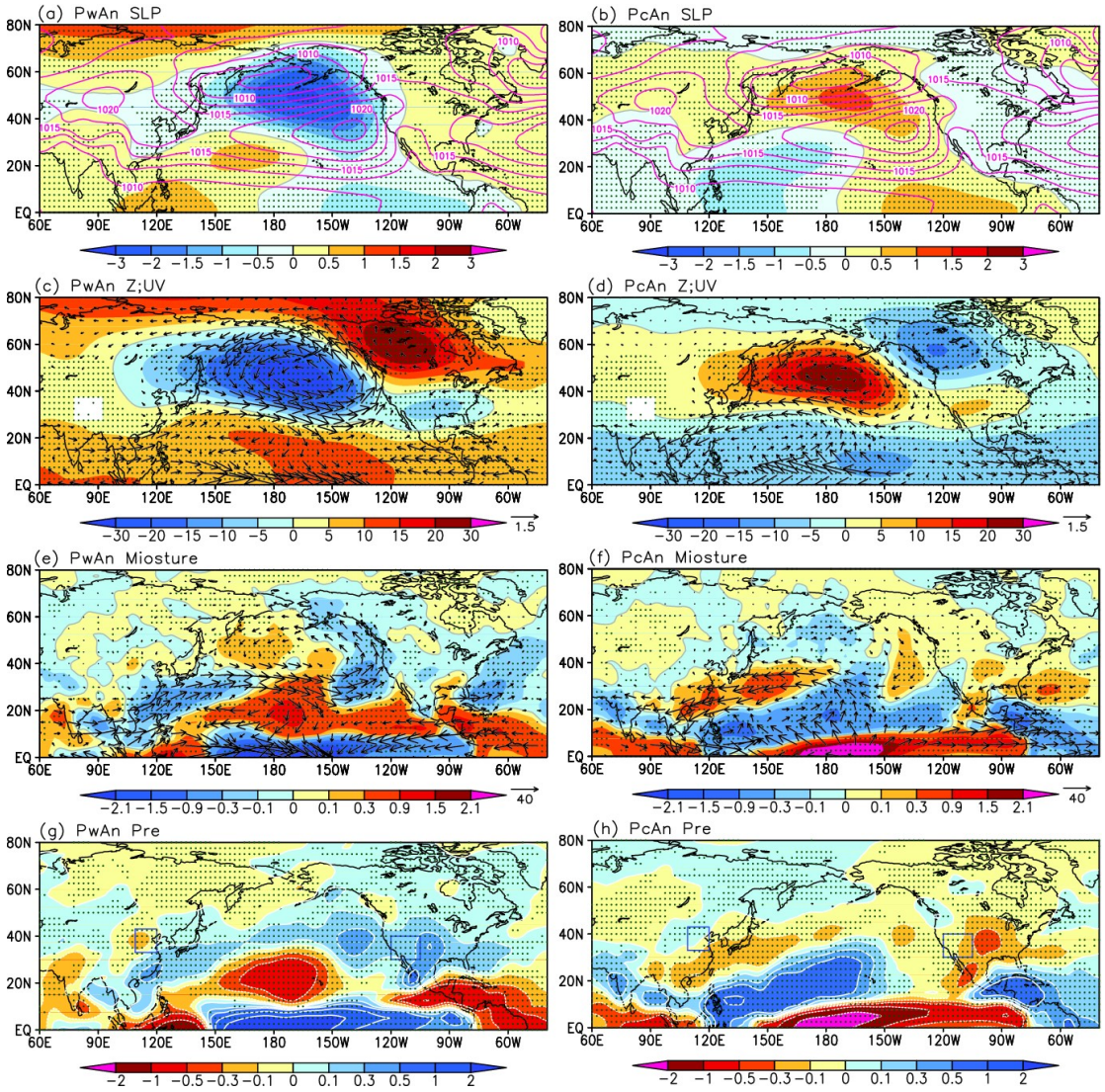

Fig. 6 Multi-model ensemble mean anomalies of annual mean (a) (b) SLP (hPa, shaded) and its climatology in PnAn (hPa, contours); (c) (d) 500-hPa geopotential height (Z, m, shaded) and 850 hPa wind (UV, m s^{-1}, vectors); (e) (f) column-integrated moisture divergence (mm day^{-1}, shaded) and moisture flux (g cm^{-1} s^{-1}, vectors); (g) (h) precipitation (Pre, mm day^{-1}, shaded), for PwAn (left column) and PcAn (right column). Note that an unequal contour interval is used to highlight the response over land. Stippling indicates areas where more than four of the five AGCMs agree on the sign.

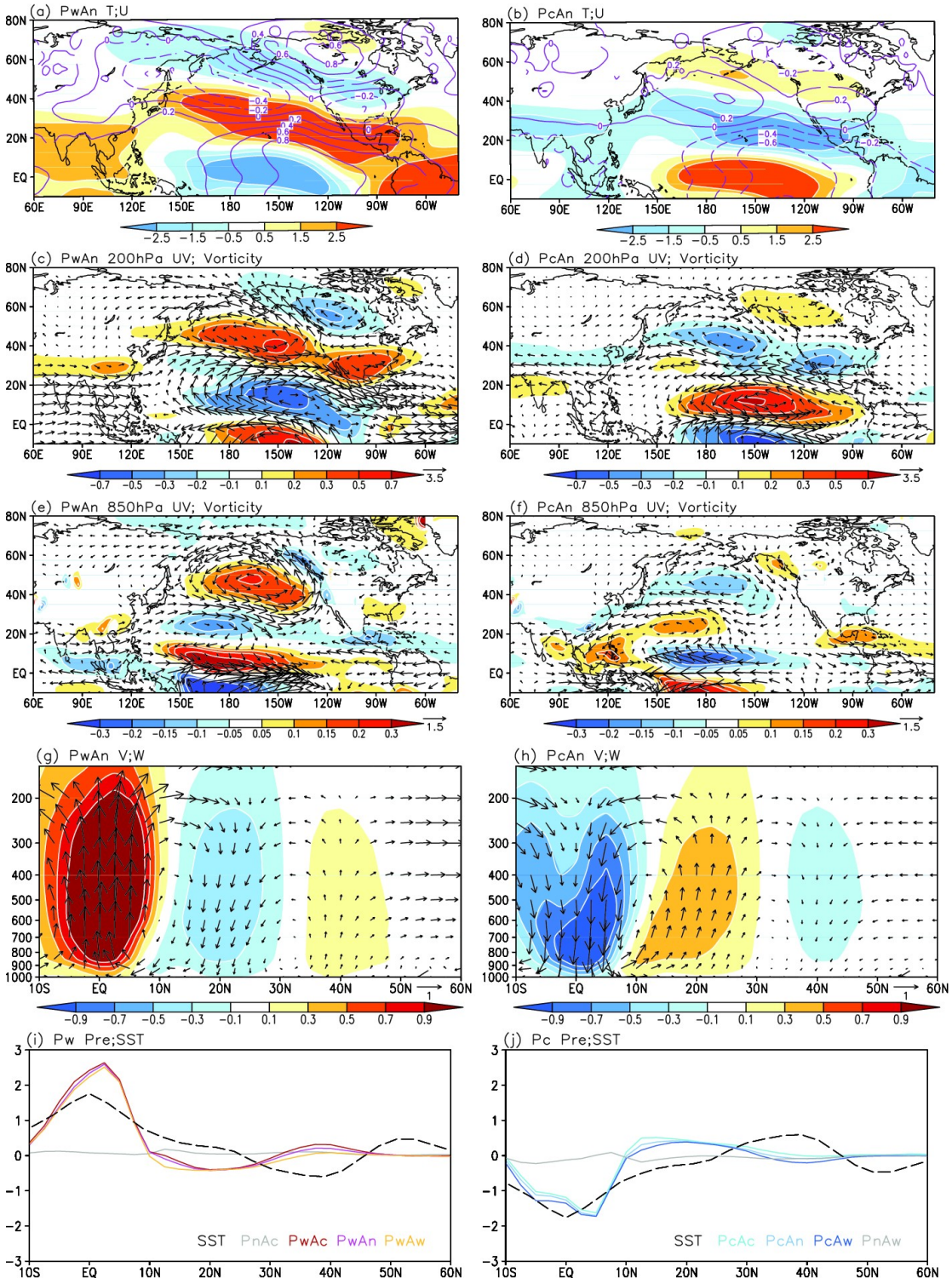

Fig. 7 Multi-model ensemble mean anomalies of annual mean (a) (b) air temperature (T, from surface to 200 hPa, contours, K) and 200 hPa zonal wind (U, shaded, m s^{-1}); wind (UV, m s^{-1}, vectors) and relative vorticity (scaled by 1e5, s^{-1}, shaded) at (c) (d) 200 hPa, and (e) (f) 850 hPa; (g) (h) meridional (V, m s^{-1}, vectors) and vertical (W, 10^{-3} m s^{-1}, shaded) circulation, and (i) (j) SST (scaled by 2, °C) and precipitation (Pre, mm day^{-1}) over the Pacific (average 150°E~120°W), for PwAn (left column) and PcAn (right

column). For convenience in comparing quantitatively the precipitation responses in different experiments, the zonal-mean precipitation anomalies in experiments with the warm (Pw) and cold IPO (Pc), as well as PnAc and PnAw, are illustrated in (i) and (j), respectively.

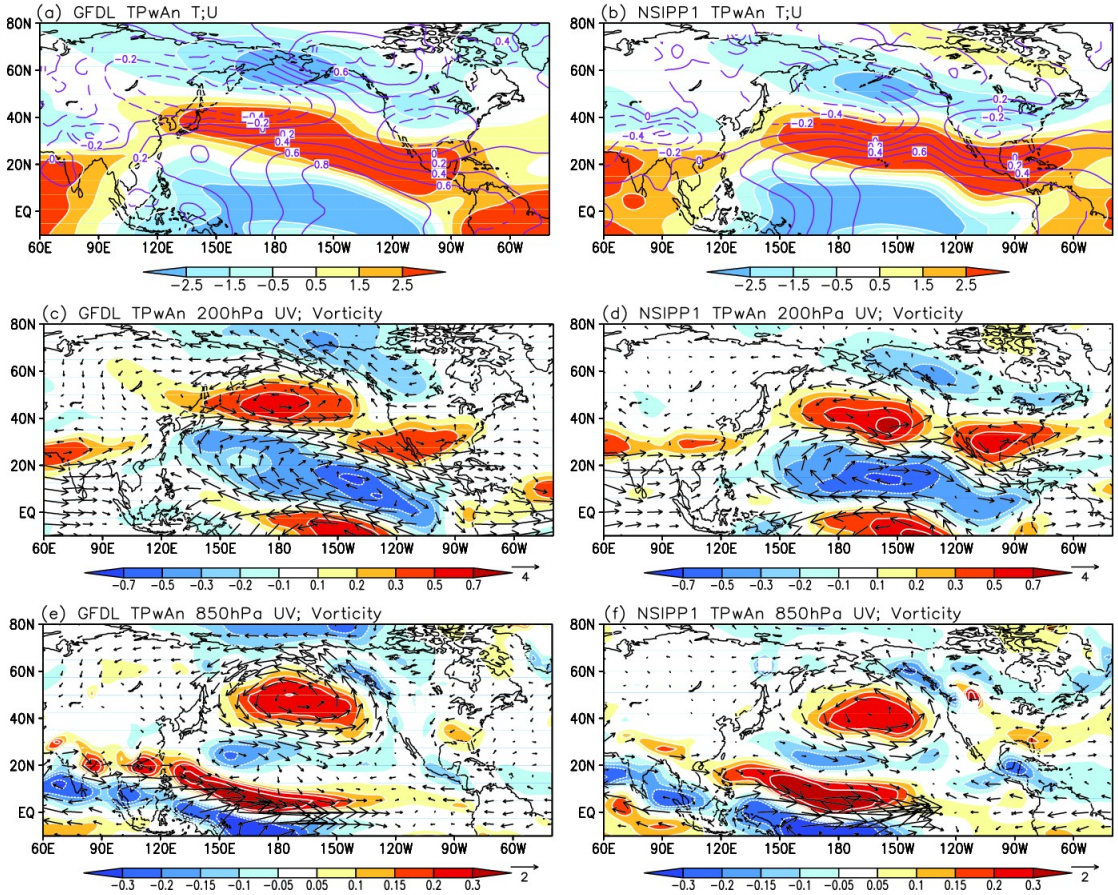

Fig. 8 Anomalies of annual mean (a) (b) air temperature (T, from surface to 200 hPa, contours, K) and 200 hPa zonal wind (U, shaded, m s^{-1}); wind (UV, m s^{-1}, vectors) and relative vorticity (scaled by 1e5, s^{-1}, shaded) at (c) (d) 200 hPa, and (e) (f) 850 hPa for TPwAn in GFDL (left column) and NSIPP1 (right column).

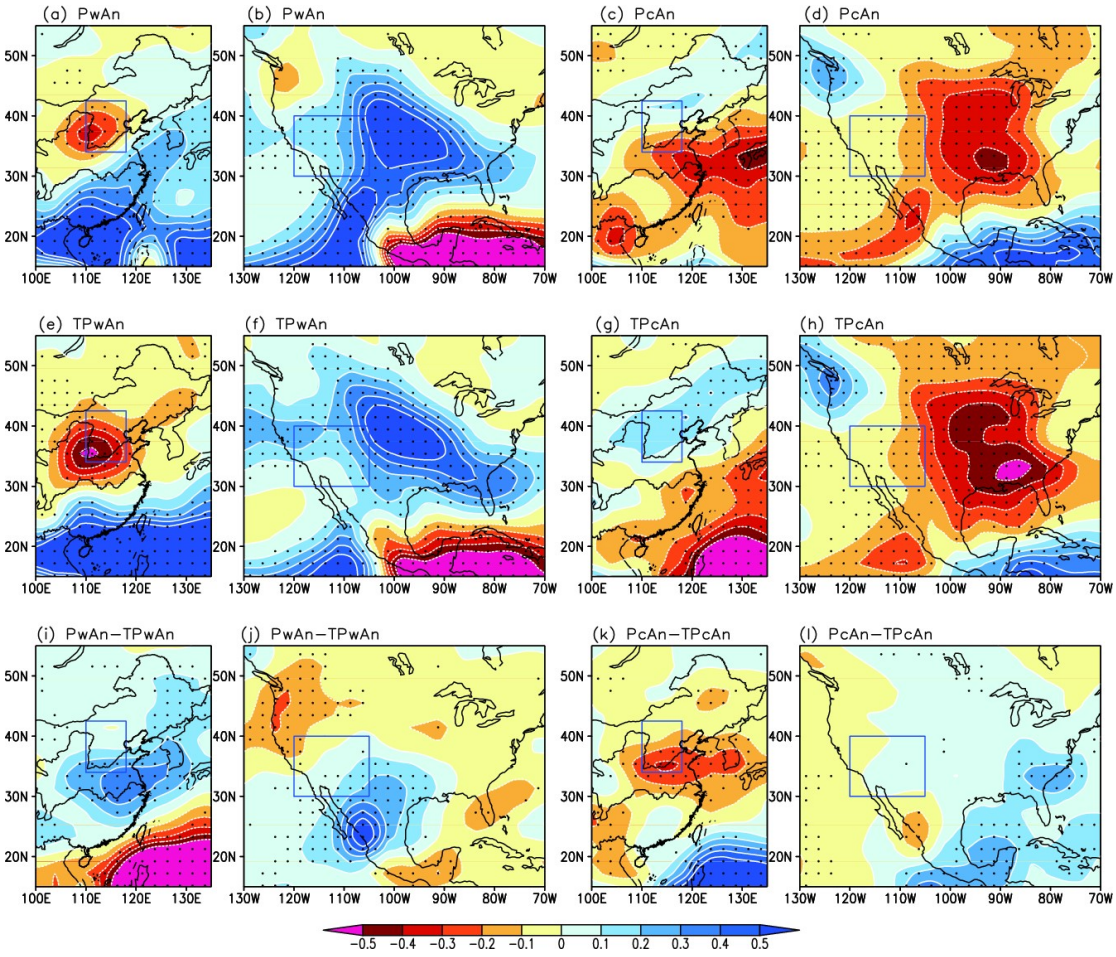

Fig. 9 Responses of annual mean precipitation (mm day^{-1}, shaded) to the Pacific pattern (PwAn and PcAn) and its tropical SST component (TPwAn and TPcAn) in GFDL. The dotted areas represent statistically significant anomalies at the 5% level.

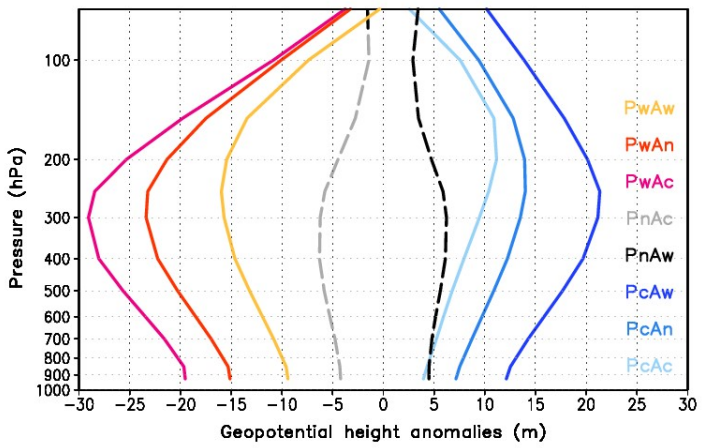

Fig. 10 Multi-model ensemble mean anomalies of annual mean geopotential height (m) over the northern North Pacific (30°-65°N, 160°E-140°W) from surface to 70 hPa.

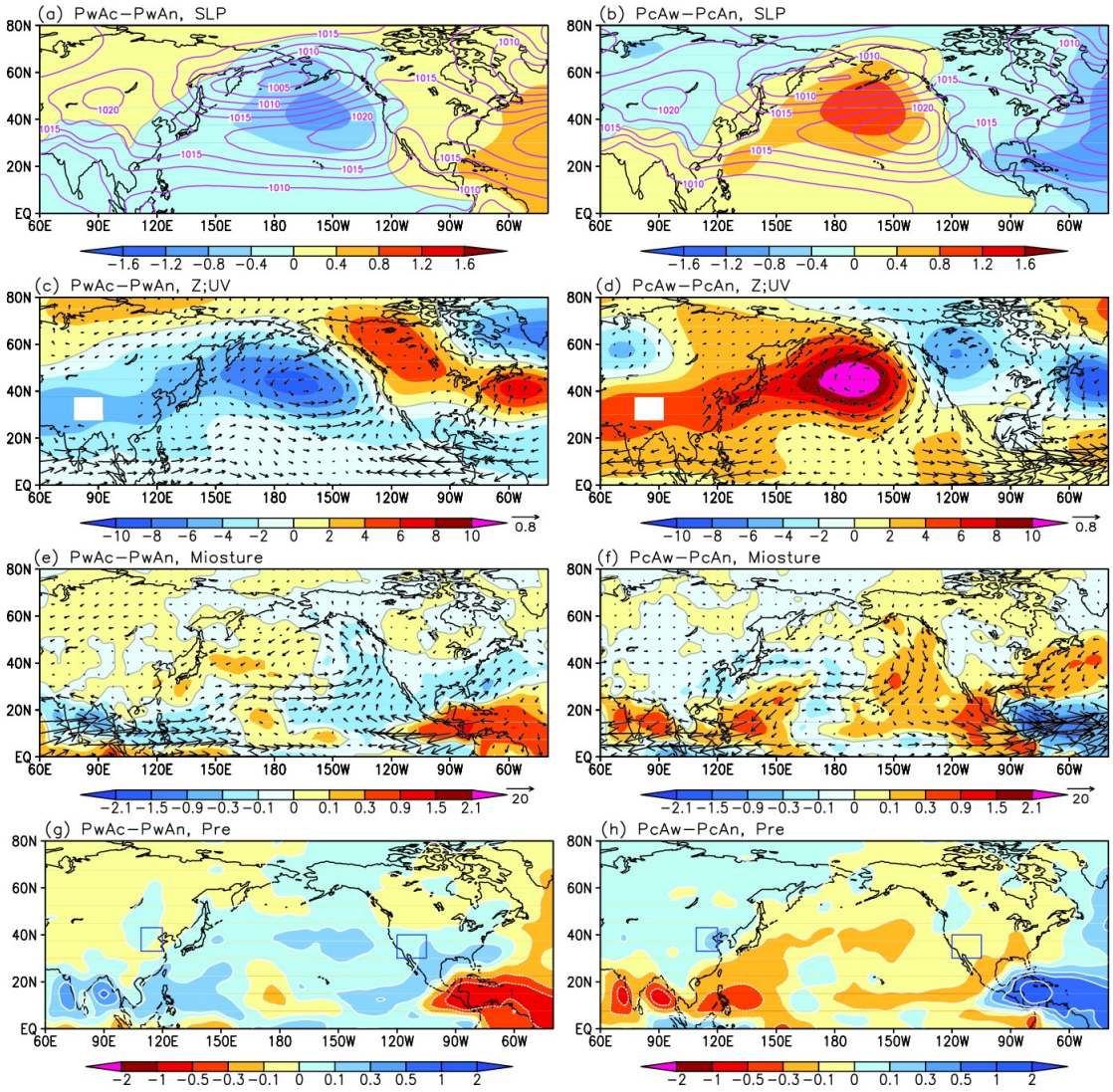

181

182 **Fig. 11** Left column: Multi-model ensemble mean differences between PwAc and
183 PwAn: (a) SLP (hPa, shaded) and SLP climatology in PwAn (hPa, contours); (c)
184 500 hPa geopotential height (Z, m, shaded) and 850 hPa wind (UV, m s^{-1}, vectors);
185 (e) column-integrated moisture divergence (mm day^{-1}, shaded) and moisture flux
186 (g cm^{-1} s^{-1}, vectors); (g) precipitation (Pre, mm day^{-1}, shaded). Right column is the
187 same as left one, but for differences between PcAw and PcAn.

188